Geophysical Journal International

Geophys. J. Int. (2026) **245,** 1–19
Advance Access publication 2026 January 30
Research Paper

https://doi.org/10.1093/gji/ggag046

Asymmetric positioning errors in GNSS time-series: a study from different world regions

Francesca Silverii [1], Emilie Klein [2], Roberto Devoti [1], Walter Szeliga [3], Sylvain Michel [2,4,5] Adriano Gualandi [6] and Elisa Trasatti [1]

[1] *Istituto Nazionale di Geofisica e Vulcanologia (INGV), Sezione Osservatorio Nazionale Terremoti,* 00143 *Rome, Italy. E-mail: francesca.silverii@ingv.it*
[2] *Laboratoire de géologie, École normale supérieure, CNRS, PSL Université, IPSL,* 75005 Paris, *France*
[3] *Department of Geological Sciences, Central Washington University,* 98926 *Ellensburg, WA, USA*
[4] *Université Côte d'Azur, Observatoire de la Côte d'Azur, IRD, CNRS, Géoazur,* 06560 *Valbonne, France*
[5] *Sorbonne Université, CNRS-INSU, Institut des Sciences de la Terre Paris, UMR* 7193, 75005 *Paris, France*
[6] *Department of Earth Sciences, University of Cambridge, CB*2 3*EQ Cambridge , UK*

Accepted 2026 January 17. Received 2026 January 14; in original form 2025 August 5

SUMMARY

Global Navigation Satellite System (GNSS) plays a fundamental role in monitoring time-dependent ground displacement. However, GNSS daily position time-series can often contain significant outliers, reaching up to several centimetres. These are likely of non-tectonic origin, and, if not properly accounted for, they can significantly impact the accuracy and dependability of the estimation of key parameters for geophysical analyses, such as long-term velocities and transient deformations. Characterizing these outliers can provide information about their possible sources and help us implement mitigation strategies. Asymmetric outliers, that is, those characterized by a primary direction, therefore occurring on one side of the mean time-series, are of particular interest since they could point to the presence of recurring or repeatable sources of error. Their key features and potential causes are, however, still not fully analysed and understood.We analyse asymmetric outliers in thousands of GNSS time-series across three regions—Central-Southern Italy, New Zealand and the Western U.S.—using data from multiple processing centres, and we reveal some persistent features among all data sets. Tens of the analysed sites exhibit hundreds of large outliers (10–50 mm), far exceeding typical position uncertainties (∼1–6 mm). Remarkably, the outliers are numerous in the horizontal component, and tend to occur near mountainous regions, with preferred direction roughly orthogonal to the local topography. The results consistency across different data sets and instrumental features suggest a physical origin for these outliers rather than a specific processing approach or instrumental configuration. Further analyses at local scales align with previous studies linking skewed position errors to uncorrected tropospheric delays driven by the coupling between atmospheric conditions and local terrain (e.g. trapped lee waves). However, other factors—such as multipath, snow accumulation on GNSS antennas or obstructed sky visibility—could also contribute to the observed asymmetric outliers. We explore mitigation strategies at both processing and post-processing stages, but further analyses and more sophisticated approaches, such as high-resolution tropospheric modelling, are needed to better understand the involved processes and achieve meaningful improvements.

Key words: Geodetic instrumentation; Satellite geodesy; Statistical methods; Time-series analysis.

1 INTRODUCTION

Thanks to its increasing precision, dense geographic distribution, and temporal continuity, the Global Navigation Satellite System (GNSS) is today an established tool for a wide range of geodetic and geophysical applications (e.g. Y. Bock & D. Melgar 2016; C. Rizos *et al.* 2020; D.S. Stamps & C. Kreemer 2024). Continuously operating GNSS networks are used to derive high-precision daily solutions with typical nominal daily repeatability of 1–2 to 4–6 mm respectively for horizontal and vertical positions (e.g. G. Blewitt *et al.* 2013; W. Bertiger *et al.* 2020). However, GNSS position time-series unavoidably exhibit stochastic fluctuations (noise) and potentially substantial position errors (outliers), ascribable to three main origins. The first is related to the satellite segment, with errors on orbits and clocks or relativistic effects. The second is due to errors associated with wave propagation through the ionosphere and troposphere, resulting in signal-path delays. Finally, errors can be related to the station itself, such as multipath effects and problems related to monument features (e.g. antenna and receiver type, monument installation). The effects of signal propagation through the troposphere, especially those related to the non-hydrostatic (the so-called 'wet') component, represent a particularly difficult challenge because of their high variability in space and time. Several processing strategies and algorithms have been developed over the years to mitigate these effects, employing different delay models, mapping functions, and gradient parameters (e.g. X. Li *et al.* 2023 and references therein). In particular, different approaches aiming at better representing the azimuthal anisotropy of the troposphere have been adopted, such as the tilting mapping function (M. Meindl *et al.* 2004), the adaptive mapping function (P. Gegout *et al.* 2011) and high-order expansion of gradients model (D. Landskron *et al.* 2017). Loosening of tropospheric constraints applied in the *GipsyX* software (W. Bertiger *et al.* 2020) has also been suggested in order to improve the precision of the estimated (vertical) position (Z.M. Young *et al.* 2024).

Position errors in GNSS time-series can range from a few millimetres to several centimetres, and can therefore impact the accuracy and dependability of GNSS data analysis and the estimation of key parameters (e.g. long-term velocities and their variations, transient signals and earthquake-related displacement). Several techniques have been developed to detect and remove position errors, but analysing them could provide important information about the possible error sources and mitigation strategies (e.g. P.J. Rousseeuw & A.M. Leroy 1987; R.A. Maronna *et al.* 2006; A. Klos *et al.* 2016; X. He *et al.* 2017; K. Gobron *et al.* 2024).

In this paper, we focused on asymmetrically distributed position errors in GNSS time-series, that is, mostly located on one side relative to the mean of the time-series, which can represent severe departure (up to a few centimetres) from the mean GNSS position (Fig. 1a). Their impact can therefore be particularly problematic in several cases. For example, when dealing with short time-series (e.g. campaign measurements) the velocity estimations can be significantly biased. If the signals of interest are of the order of a few millimetres in displacement and short lived (a few days), the effect of these outliers may be even more detrimental, leading either to false identification or to a missed identification of transient signals, such as slow slip events on faults. These outliers can be problematic also when the signal of interest relies on a few measurement points, as in the case of coseismic displacement estimation.

So far, a few studies specifically analysed these 'dripping outliers' in multiple GNSS time-series and they proposed as primary cause the tropospheric delay associated with coupling between atmosphere and local topography, such as the formation of tropospheric lee waves (e.g. S. Shimada *et al.* 2002; K. Materna 2014; W.M. Szeliga *et al.* 2022). These are a type of atmospheric gravity waves forming when stably stratified air flows over steep uneven topography, creating turbulence downstream, with the most intense ones typically associated with long and narrow ridges (R.S. Scorer 1949; D.R. Durran 1986; D. Durran 2003). In particular, horizontally propagating waves, also known as trapped or stationary lee waves, form when airflow leads to atmosphere oscillations downstream from the mountain for restoring the hydrostatic equilibrium. Trapped lee waves can be associated with the formation of rows of parallel clouds. By creating (local) nonlinear inhomogeneity in the troposphere, which are not accounted for in the routine procedures of tropospheric delay correction implemented in GNSS processing, this phenomenon would cause degradation of GNSS positioning accuracy, resulting in position errors. In the early 2000s, studies focusing on the Izu Peninsula in Japan revealed that lee waves typically forming in this region caused significant systematic position errors in GNSS time-series (S. Shimada *et al.* 2002; H. Seko *et al.* 2004; R. Ichikawa *et al.* 2004). These errors were especially pronounced in the horizontal GNSS components exhibiting aligned directions generally perpendicular to the local topography and the lee wave patterns. Using high-resolution numerical weather models to simulate lee wave conditions, these authors demonstrated that systematic horizontal position errors have directions dependent on the GNSS site distance from the mountain generating the lee waves, and that lee waves can also cause alternating vertical position errors. K. Materna (2014) found that approximately 5–10 per cent of GNSS stations in the Western United States, primarily located near mountainous areas, exhibited strongly asymmetrically distributed ('skewed') outliers. Focusing on the San Bernardino Valley in Southern California—an area prone to trapped lee waves—W.M. Szeliga *et al.* (2022), W.M. Szeliga & L. Grey (2023), L. Grey (2024) and W.M. Szeliga & L. Grey (2026) found that horizontal GNSS anomalies often coincided with atmospheric conditions favourable for trapped lee wave formation, pointing toward nearby topography, with amplitude decreasing with distance from it, and showing a slight correlation with the lee waves' duration and downstream extent.

The aforementioned studies primarily concentrate on localized regions and limited time periods, examining time-series solutions derived from a single processing method. Systematic analyses are still lacking to determine whether asymmetric outliers exhibit consistent characteristics across multiple regions, processing strategies and instrumental features, and if those are potentially attributable to a common underlying cause. Here we systematically analyse time-series data from thousands of GNSS stations across three regions (Central-Southern Italy, New Zealand and Western U.S.), each encompassing both lowland (planar) and mountainous terrains, and monitored by dense continuous GNSS networks. For each region, we consider the time-series resulting from different processing software and processing centres and we apply a skewness analysis. We observe that several sites in the selected regions show numerous (tens-to-hundreds) large, asymmetrically distributed, positioning data errors (10–50 mm). We then focus on three smaller areas, one

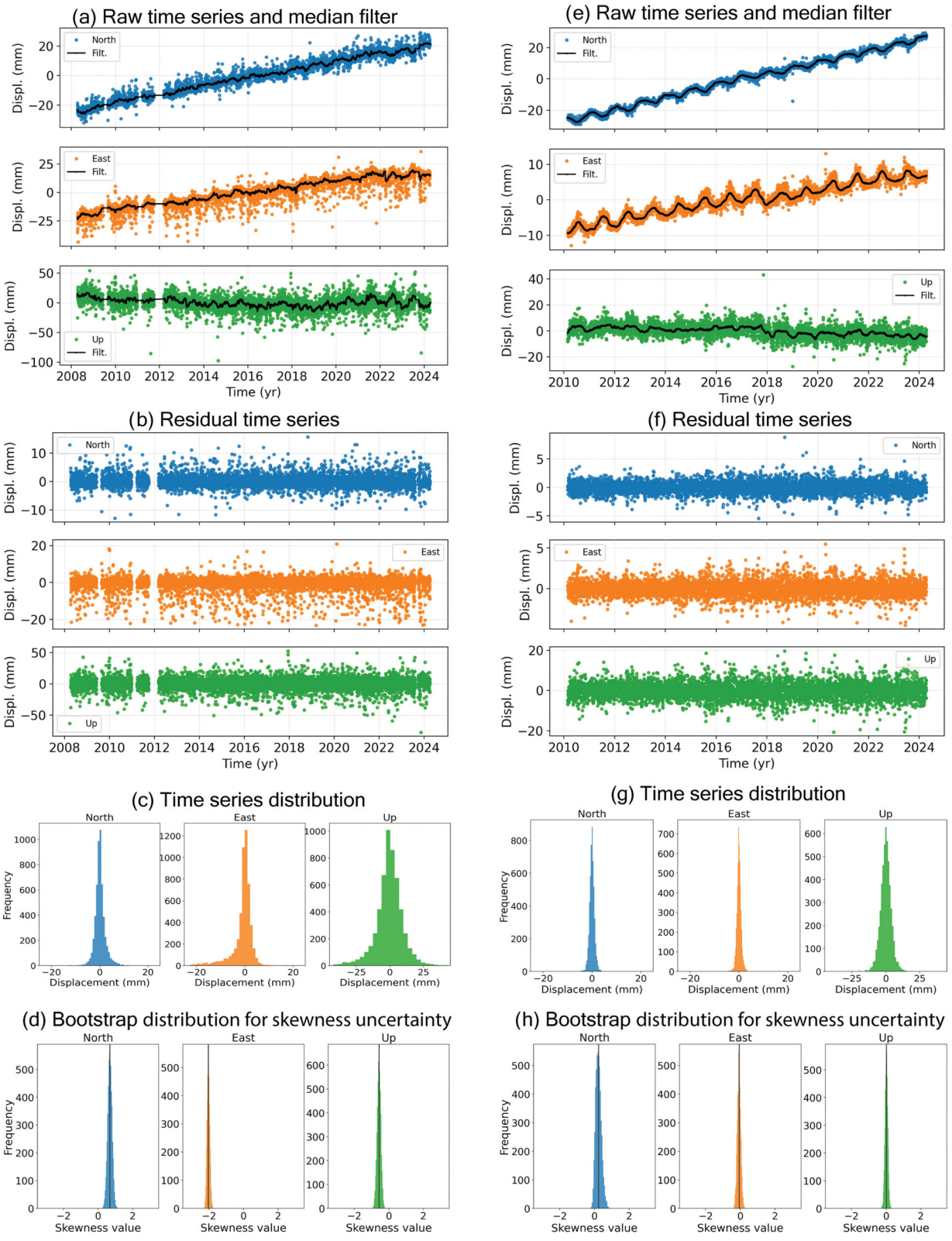

Figure 1. Main steps of time-series post-processing and skewness estimation. Panels (a) and (e) show the raw position time-series for two different GNSS sites, one with skewed time-series (station LPEL, panel a) and one with non-skewed time-series (station USAL, panel e). Both stations are located in Central-Southern Italy and the time-series belong to the *INGV_GIPSY* data set (Table 1). Panels (b) and (f) show the residual filtered time-series, with removed linear trend, offsets, seasonal and transient behaviours and very large residuals. Panels (c) and (g) show the histograms, indicative on the probability density functions, associated with the time-series of panels (b) and (f). The skewness for each filtered time-series is calculated, and its significance is addressed by the bootstrap distribution shown in panels (d) and (h), where skewness values significantly different from 0 are found for LPEL (panel d), but not for USAL (panel h).

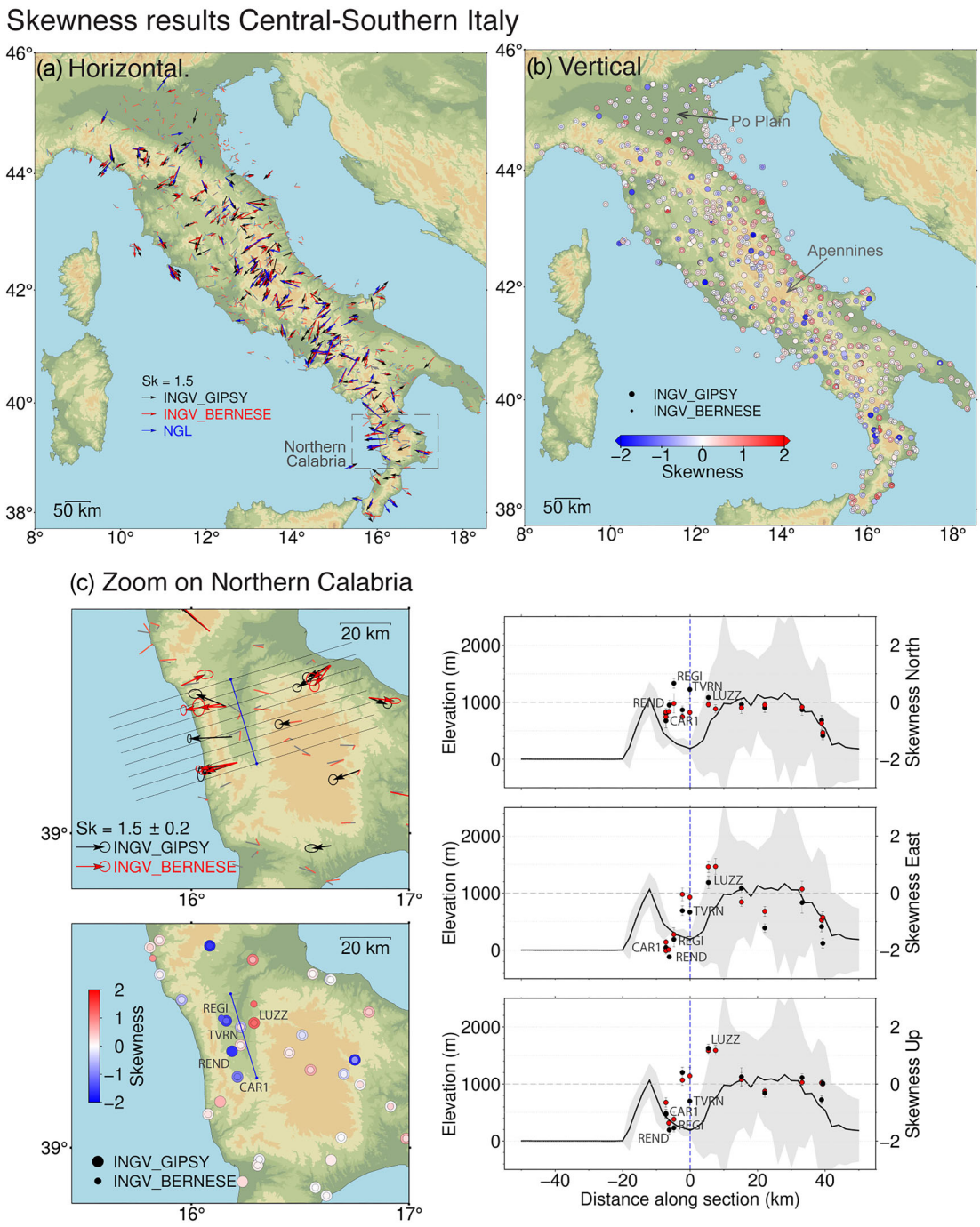

Figure 2. Skewness analysis results for Central-Southern Italy. The geographical locations mentioned in the text are indicated in the maps. (a) Horizontal skewness results for three analysed data sets; the darker and lighter vectors highlight sites with skewness amplitude respectively higher and lower than 1. (b) Vertical skewness results; for the sake of plot clarity, only two of the three data sets are shown. (c) Skewness analysis results zoomed on Northern Calabria area (dashed rectangle in panel a). For plot clarity, only two of the three data sets are displayed. Horizontal skewness is displayed with associated uncertainty values (60 per cent confidence interval ellipse). The plots on the right display skewness values (red and black circles) along a cross-section (grey and blue lines in the maps), and stacked and median topography along the cross-section profiles (black line and grey stripe).

for each studied region, in order to assess common and robust features of this kind of position errors and speculate about their possible causes and mitigation strategies.

The paper is organized as follows. First, we introduce the data in Section 2. We present the applied skewness method and the related results in Sections 3 and 4, followed by discussions in Section 5 and final remarks in Section 6.

2 DATA

In this study, we consider raw GNSS position time-series for three world regions: peninsular Central-Southern Italy (8°E to 18.5°E, 37.5°N to 45.5°N, Fig. 2), New Zealand (166°E to 179°E, 34°S to 48°S, Fig. 3) and Western United States (232°W to 246.5°W, 32°N to 46.5°N, Fig. 4). In order to characterize the main features of the positioning errors in GNSS time-series,

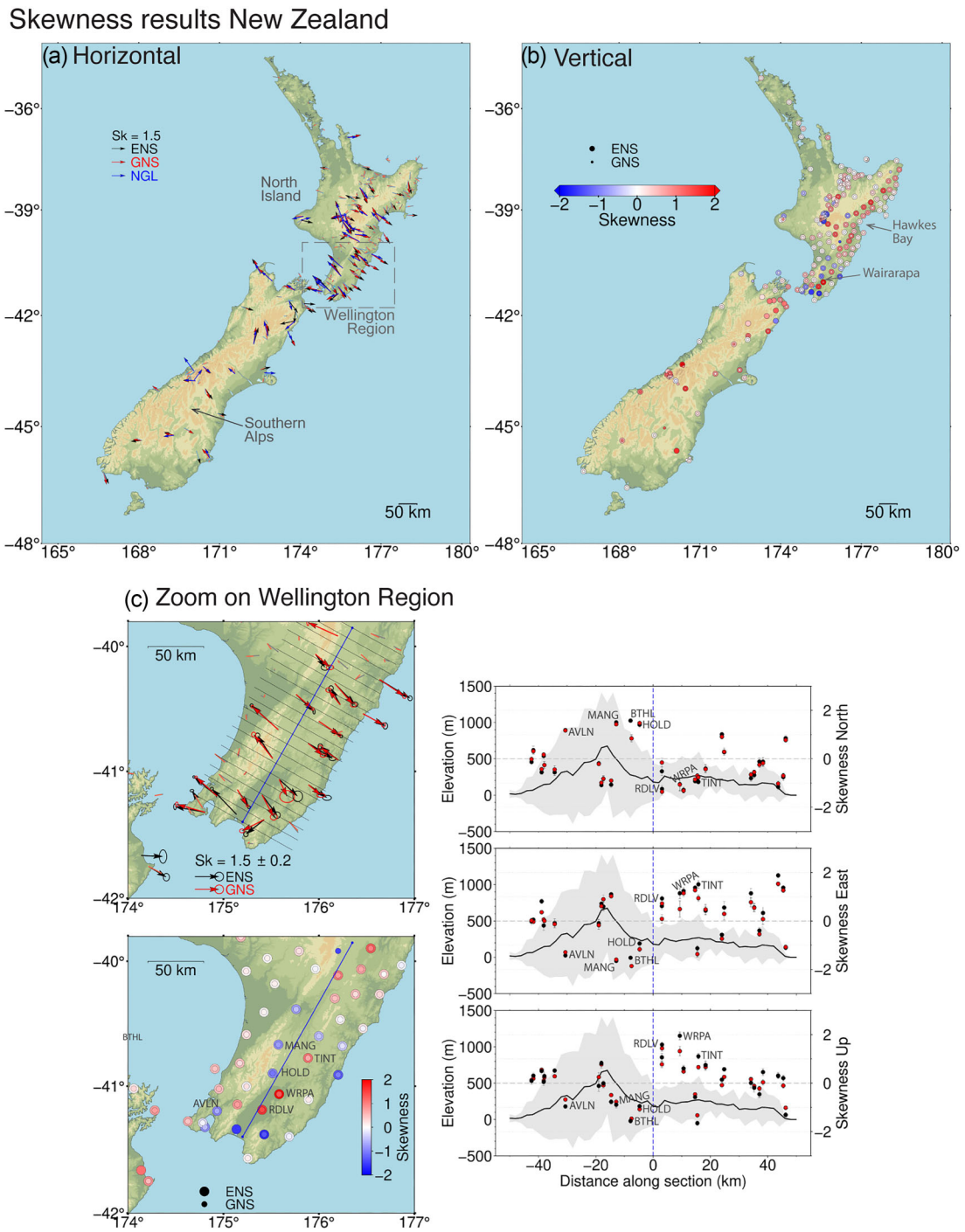

Figure 3. Skewness analysis results for New Zealand. All plots are analogous to Fig. 2. Panel (c) represents skewness analysis results zoomed on Wellington Region (dashed rectangle in panel a).

and to test the robustness of the obtained results, we analyse several GNSS data sets. In particular, for each region we consider data sets from three different processing centres, implying different processing software and related settings, such as positioning methods, error correction/mitigation techniques and reference frames. We use both (i) publicly available time-series provided by Nevada Geodetic Laboratory–University of Nevada (NGL), GeoNet–GNS Science, Scripps Institution of Oceanography's Orbit and Permanent Array Center (SOPAC) and NASA Jet Propulsion Laboratory (JPL), and (ii) time-series processed at Istituto Nazionale di Geofisica e Vulcanologia (INGV) and Ecole normale superiéure (ENS). For each region, we collect hundreds of daily time-series, updated until the end of 2022/beginning of 2024. These time-series are characterized by various duration (a few years to a few decades) and presence of data gaps. For our analysis, we therefore select time-series with at least three years duration and 60 per cent completeness (defined as the ratio between the actual and the expected number of data points based

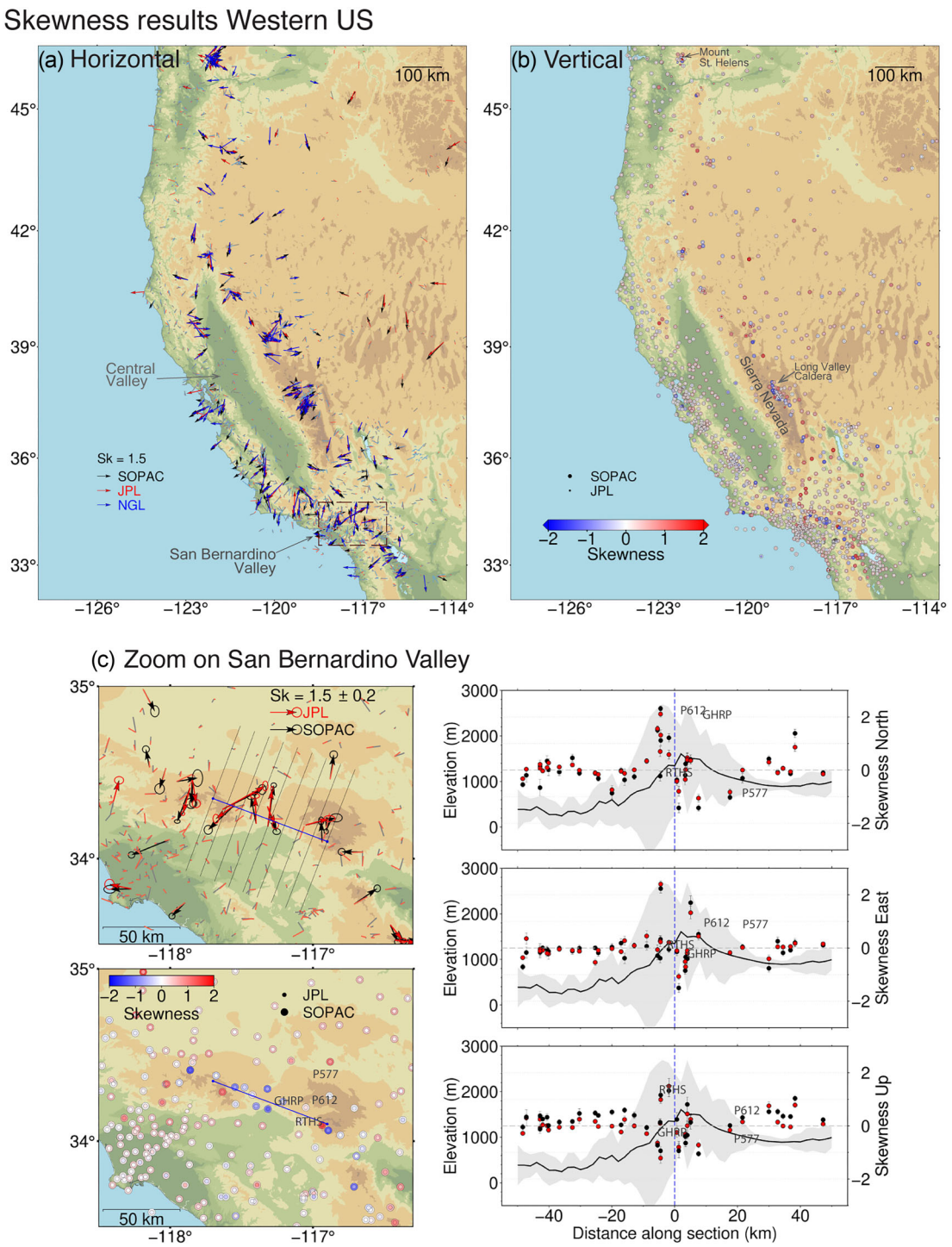

Figure 4. Skewness analysis results for Western U.S.. All plots are analogous to Fig. 2. Panel (c) represents skewness analysis results zoomed on San Bernardino Valley (dashed rectangle in panel a).

on daily sampling frequency). Details on processing software, reference frame and number of sites for each data set we use are summarized in Table 1. Supplementary Table S1 of the Supplementary Material outlines the employed tropospheric correction strategies for each data set. Further information about data sources and data availability are provided in the *Data availability* Section.

Furthermore, in order to check whether the asymmetric positioning errors could be related to specific station instrumentation features, we gather the available information about monumentation and instrumentation of the analysed GNSS stations (e.g. receiver and antenna type, monument foundation antenna height) from several data sources (details in Supplementary Table S2 of the Supplementary Material).

Table 1. Information about the GNSS time-series data sets used in this study.

Processing centre	Processing software (positioning method[a])	Ref. frame	#Sites (all/sel.[b]) [updated until MM-YYYY]
Central-Southern Italy			
INGV	Gipsy-Oasis II (PPP)	IGb14	695/622 [04-2024]
INGV	Bernese (DD)	ITRF2014	688/568 [10-2023]
NGL	GipsyX (PPP)	IGS14	527/409 [04-2024]
New Zealand			
ENS	GAMIT-GLOBK (DD)	ITRF2014	182/180 [12-2022]
GeoNet - GNS Science	GAMIT-GLOBK (DD)	ITRF2008	174/174 [12-2022]
NGL	GipsyX (PPP)	IGS14	236/211 [04-2024]
Western U.S.			
JPL	GipsyX (PPP)	IGS14	1312/1254 [11-2023]
SOPAC	GAMIT-GLOBK (DD)	ITRF2014	1269/1144 [06-2023]
NGL	GipsyX (PPP)	IGS14	1991/1452 [06-2023]

[a]Precise Point Positioning (PPP); Double Differences (DD)
[b]Selected: time-series duration ≥3 yr and time-series completeness ≥60 per cent

3 METHODS

We employ a skewness analysis approach—similarly to K. Materna (2014)—in order to identify the GNSS sites showing highly asymmetric position errors and the related spatiotemporal features.

We first implement a pre-processing step consisting in computing and subtracting a 30-d window median filter on each time-series (North, East, Up) in order to remove long-term trends, seasonal and transient signals, and offsets (Figs 1a and e). The remainder consists of daily residual position time-series centred on zero. Additionally, we remove very large residuals, which might represent isolated bad data and could bias the skewness results. This step is particularly important given the large number of time-series involved in our study, making it impractical to inspect each one individually. In particular, we discarded residuals higher/lower than eight times the time-series interquartile range (IQR), which accounted for <3 per cent of the total time-series data points. The value of this multiplicative factor (8) was chosen to compromise between removing strong and isolated outliers—which could severely bias the analysis results (i.e. resulting in very high and randomly distributed skewness values)—and avoiding removing too many (asymmetric) outliers—which would lead to strongly underestimated skewness values. These effects can be seen in tests made using more (6) and less (20) conservative multiplicative factor values (Supplementary Fig. S1 of the Supplementary Material). Hereafter we refer to the time-series resulting from this pre-processing step as 'residual time-series' (Figs 1b and f).

We then compute the normalized skewness of each residual time-series to provide a statistical measure of its asymmetry. We expect a non-null skewness when the distribution is characterized by a longer tail either right or left of its peak. This, in our case, would correspond to the presence of predominant positive or negative outliers in the residual time-series (Figs 1c and g). To estimate an uncertainty associated with the skewness results, we employ the bootstrap method (B. Efron & R. Tibshirani 1986) with 5000 repetitions. This consists in creating synthetic data sets by randomly selecting N points from the original data set, where each point is selected independently and can be chosen more than once. In our case each data set is a component (North, East, Up) of the residual time-series of a GNSS site, N being the number of data in the time-series. The skewness is then recomputed for each new sample of N points (i.e. for each synthetic time-series). By implementing this process many times, a distribution of skewness values is constructed for each residual time-series and a statistical uncertainty value can be estimated from the distribution variance (Figs 1d and h).

We implement the skewness computation separately for each component (North, East, Up), resulting in a 3-D 'skewness vector' and associated uncertainty for each GNSS site. Having removed the most extreme outliers, this vector can be loosely interpreted as the tendency for (asymmetric) outliers at each site, with direction and magnitude roughly representing the direction in which outliers are most likely, and the likelihood of outliers in that direction, respectively. Since high skewness value does not necessarily mean frequent outliers, as a further information we also compute the number of outliers for each residual time-series by selecting the data points exceeding 1.5 times IQR.

4 RESULTS

4.1 Skewness analysis results

The outcome of the skewness analysis for the three areas and three data sets is represented synthetically in Figs 2, 3 and 4 and separately (for each area and each data set) in Supplementary Figs S2–S10 of the Supplementary Material. Fig. 5 and Supplementary Table S3 of the Supplementary Material display the distribution (number and percentage) of sites across three groups defined by the absolute amplitude of horizontal and vertical skewness (low: skewness < 0.5; intermediate: $0.5 \leq$ skewness <1; high: skewness ≥ 1).

For each analysed area, the results associated with different data sets, and therefore different processing centres, are mostly consistent about the percentage (differences generally lower than 10 per cent) and location of sites with high outliers' asymmetry and the associated skewness values. The case exhibiting the greatest variation is New Zealand, with up to 30 per cent difference in low- and high-skewness sites between *ENS* and *NGL* solutions. In all cases (geographical regions and data sets), most (60–95 per cent) of the sites are characterized by low and intermediate skewness, but a significant number (tens) of highly skewed stations exist (skewness up to 2.5). Furthermore, the number of highly skewed sites is about 2 to 4 times higher for the horizontal components with respect to the vertical one.

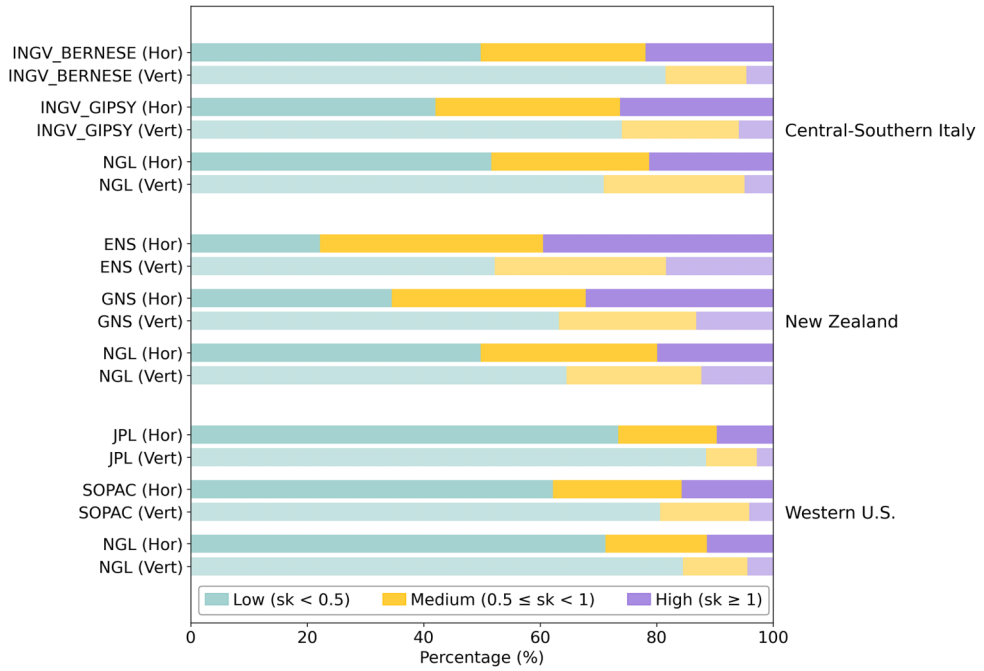

Figure 5. Percentage of sites associated with different values of horizontal and vertical skewness amplitude (with respect to the total number of selected sites for each data set). The corresponding numerical values are displayed in Supplementary Table S3 of the Supplementary Material.

The spatial distribution of skewness highlights some notable features which are common to the three analysed regions, particularly regarding the horizontal components. The majority of the sites characterized by high horizontal skewness are located close to/in mountainous areas, with skewness direction mostly perpendicular to the main topography orientation (e.g. along the main mountain ranges of Central-Southern Italy, of eastern North Island in New Zealand and of California in Western U.S.). On the contrary, sites located in large planar areas (e.g. Po Plain in Northern Italy, and Central Valley in California) show systematically lower skewness values (Figs 2a, 3a and 4a, and panels a, b in Supplementary Figs S2–S10 of the Supplementary Material).

The results for the vertical component are less clear, showing more randomly distributed skewness values and a lower number of high skewness sites (Figs 2b, 3b and 4b, and panel c in Supplementary Figs S2–S10 of the Supplementary Material). In some cases, however, high (positive/negative) vertical skewness values are found at the sites also showing high horizontal skewness values and located close to mountainous areas. This is particularly visible in New Zealand and Western U.S.. We afterwards highlight some potentially interesting features focusing on smaller scales, as described in Section 4.2.

The estimated number of outliers (defined as positioning data exceeding 1.5 times the IQR; panels d–f in Supplementary Figs S2–S10 of the Supplementary Material) show that the sites with high skewness are generally characterized by numerous (tens to hundreds) outliers. This provides a further confirmation of the robustness of skewness results, that is, large skewness values generally not being simply due to few singletons.

4.2 Local-scale focus–troposphere behaviour

After identifying the main common features of skewed time-series at large scales, we focus on three local areas to conduct a more detailed analysis of the potential underlying causes. We select three mountainous areas characterized by the presence of highly skewed GNSS sites and rather simple topography (i.e. long and narrow ridges): the northern section of Calabria Region (Central-Southern Italy), Wellington Region (New Zealand) and San Bernardino Valley, California (Western U.S.) (contoured areas in Figs 2a, 3a and 4a). In Supplementary Fig. S11 of the Supplementary Material we collect examples of residual time-series at different sites in the selected areas. A closer look to the skewness analysis results for the selected areas (Figs 2c, 3c and 4c) highlights some common features: (i) presence of valleys close to mountain ranges, (ii) presence of stations lying in the immediate lee of the mountain range characterized by skewed horizontal position outliers consistently oriented quasi-perpendicularly to the nearby mountains; (iii) skewness values lowering at sites farther from the mountain range. The distribution of vertical skewness is more scattered, but it also shows higher values at sites closer to the mountain range. Furthermore, particularly in the Northern Calabria and Wellington area, sites located within the valley at different distances from the mountain range have opposite horizontal skewness direction and alternating sign (upward/downward) in vertical skewness [e.g. REND versus LUZZ, Northern Calabria, Fig. S11(A.1); MANG versus RDLV, Wellington area, Supplementary Fig. S11(B.1)].

In order to identify potential correlations between the behaviour of the atmosphere and large position anomalies, we collect the tropospheric products provided at 5 min frequency by *NGL* (http://geodesy.unr.edu/gps_timeseries/README_trop2.txt) at selected epochs and for all the available sites in the three areas, and we gather daily satellite imagery from the Moderate Resolution Imaging Spectroradiometer (MODIS) instrument on NASA's Terra and Aqua satellites (https://worldview.earthdata.nasa.gov/). We select 4 d for each area, two of which showing anomalous horizontal positions. Note that, since for this analysis we are dealing with few sites—and it is therefore doable to check them singularly for the presence of singletons—in order to avoid removing meaningful data we considered time-series without discarding the data exceeding eight times

IQR (Section 3). Fig. 6 shows maps of hourly sampled tropospheric products (zenith wet delay—ZWD—and north and east tropospheric gradients) at each site, together with the corresponding residual daily position from the *NGL* data base (Section 2).

In the Northern Calabria and Wellington Region cases, anomalous position days (Figs 6a.2, a.4, b.3 and b.4) show higher values of horizontal gradients (up to about 3–4 mm, compared with $\leq$ 2 mm in normal days) and presence of lee waves, appearing as closely spaced rows of clouds parallel to the mountain range. The ZWD does not show clear features in anomalous days, but results in higher values (up to 150–250 mm) on days with dense cloud cover (Figs 6a.1, b.2 and b.3). For the San Bernardino Valley case, due to the high station density, we restrict the analysis to sites within a stripe of about 80 $\times$ 150 km^2 across San Bernardino Mountain. We select two days known for lee waves formations (2018 December 29 in Fig. 6c.1, and 2019 January 22 in Fig. 6c.4) (W.M. Szeliga *et al.* 2022; W.M. Szeliga & L. Grey 2023; L. Grey 2024). Due to the arid climate, lee waves formations in this area are usually not associated with cloud formations, as also testified by the clear sky images from MODIS. These days show anomalous displacement values and relatively high values of horizontal gradients (up to 2 mm) at the sites south of San Bernardino Mountains. These sites generally show higher values of horizontal gradients and ZWD also in cloudy days (Fig. 6c.2).

The survey of MODIS images we inspected in the Northern Calabria and Wellington Regions show linear cloud formations on the east of the mountain ranges, with four to ten crests of lee waves with typical wavelengths of 10–15 km. Although lee waves are seen in satellite images on the selected outlier days, it is important to note that MODIS observations offer only a partial view of lee wave activity in the studied regions. MODIS-equipped satellites indeed sample a specific location twice per day, providing the possibility that lee wave activity at other times could go undetected. Additionally, certain conditions, as extremely cloudy or extremely clear weather, can prevent lee waves from being visible as parallel cloud formations, as for the case of San Bernardino Valley.

In summary, the features observed at the selected epochs suggest that days with anomalous displacement are associated with lee-wave formations, and relatively higher horizontal gradients, but not necessarily higher ZWD values.

5 DISCUSSION

The analysis performed on three world regions (Western U.S., New Zealand and Central-Southern Italy) and considering different data sets highlights some main common features of the spatiotemporal distribution of asymmetric outliers in GNSS time-series: (i) presence of tens of GNSS sites with high-skewness ($\geq$1) residual time-series, particularly in the horizontal components (2–4 times more numerous than the vertical); (ii) majority of sites with high horizontal skewness located close to/in mountainous areas; (iii) horizontal position errors mostly directed roughly perpendicularly to the closest mountain; (iv) noisier results for the vertical component, but alternating upward–downward pattern found at local scales in some cases. Hereafter we discuss about the possible causes of the observed skewed time-series and their features.

5.1 Possible causes

5.1.1 Instrumental features and different data sets

The spatial distribution of the available instrumental features (Supplementary Table S2 and Supplementary Figs S12–S14 of the Supplementary Material) shows a large variability between sites. Even if not all collected monument features are available at all sites, there is no obvious correlation between a specific monument feature and high skewness values. This can be observed even more clearly by focusing on smaller scales (Supplementary Figs S15–S17 of the Supplementary Material). Several studies have analysed the possible relation between noise in GNSS time-series and the corresponding sites monumentation and instrumentation features (e.g. J. Beavan 2005; J. Langbein & J.L. Svarc 2019). The stability and design of the GNSS monument and the quality and calibration of the GNSS receivers and antennas can indeed significantly affect the noise characteristics of the time-series. The comparison between the collected information about monumentation and instrumentation and the results of our analysis suggest that specific instrumental features are most likely not the main cause of skewed outliers.

For each analysed region, the results of skewness analysis obtained from data sets resulting from different processing centres reveal a clear consistency (Section 4.1). The minor existing differences in skewness values and outliers number between the different processing centres can be ascribed to diverse factors. Among these, the variability in the time-series time-span, the possible presence of remaining singleton outliers and the time-series daily scatter, that is, how spread the data points are over time, with higher scatter possibly resulting in lower skewness results. The latter factor could explain part of the variability observed between the results of the *NGL* and *ENS* or *GNS* data set for the New Zealand case (Fig. 5 and Supplementary Table S3 of the Supplementary Material; an example of time-series comparison is represented in Supplementary Fig. S11(B.2) of the Supplementary Material). Central-Southern Italy and New Zealand result in higher percentage of horizontal high-skewness sites (20–40 per cent) compared to Western U.S. (9–15 per cent). This can be ascribed to the smaller and mostly mountainous area of the former, whereas the Western U.S. data sets cover a much larger area encompassing both mountainous and large plain regions. We can therefore conclude that the occurrence of asymmetric outliers is mostly independent from the different processing approaches used to produce the data sets considered here.

5.1.2 Tropospheric delay hypothesis

As introduced in Section 1, some previous studies have indicated tropospheric inhomogeneities, and in particular the phenomenon of trapped tropospheric lee waves, as the possible cause of skewed position errors in GNSS time-series (S. Shimada *et al.* 2002; H. Seko *et al.* 2004; R. Ichikawa *et al.* 2004; K. Materna 2014; W.M. Szeliga *et al.* 2022; W.M. Szeliga & L. Grey 2023; L. Grey 2024; W.M. Szeliga & L. Grey 2026). The locations where we detect skewed position errors are mountain areas where lee waves formations are often observed, such as the Apennines in Italy (https://www.aeronautica.difesa.it/wp-content/uploads/2023/01/RIVISTA_2_2021_FIN.pdf), the Sierra Nevada and the San Bernardino Valley in Western U.S. (K. Materna 2014; W.M. Szeliga *et al.* 2022; W.M. Szeliga & L.

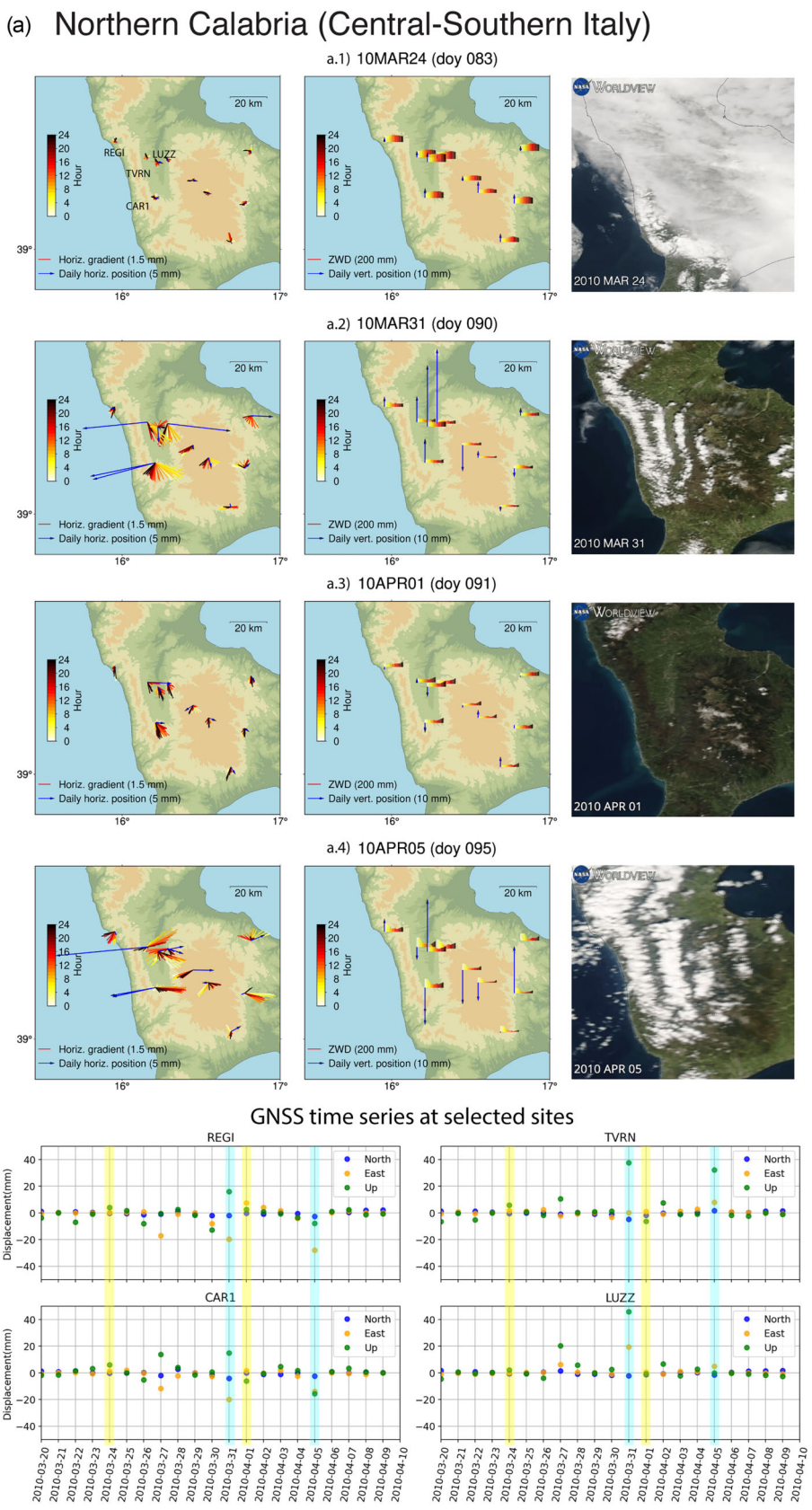

Figure 6. Local-scale maps of hourly tropospheric parameters values at four selected days. First column: horizontal tropospheric gradients (bars oriented according to the E-W and N-S components), and horizontal daily position (*NGL* data set, blue arrows). Second column: ZWD (vertical bars), and vertical daily position (*NGL* data set, blue arrows). Third column: MODIS satellites images (NASA Worldview). Bottom: residual time-series including the selected 'regular' and 'outliers' days (respectively yellow and cyan vertical bars) of some sites.

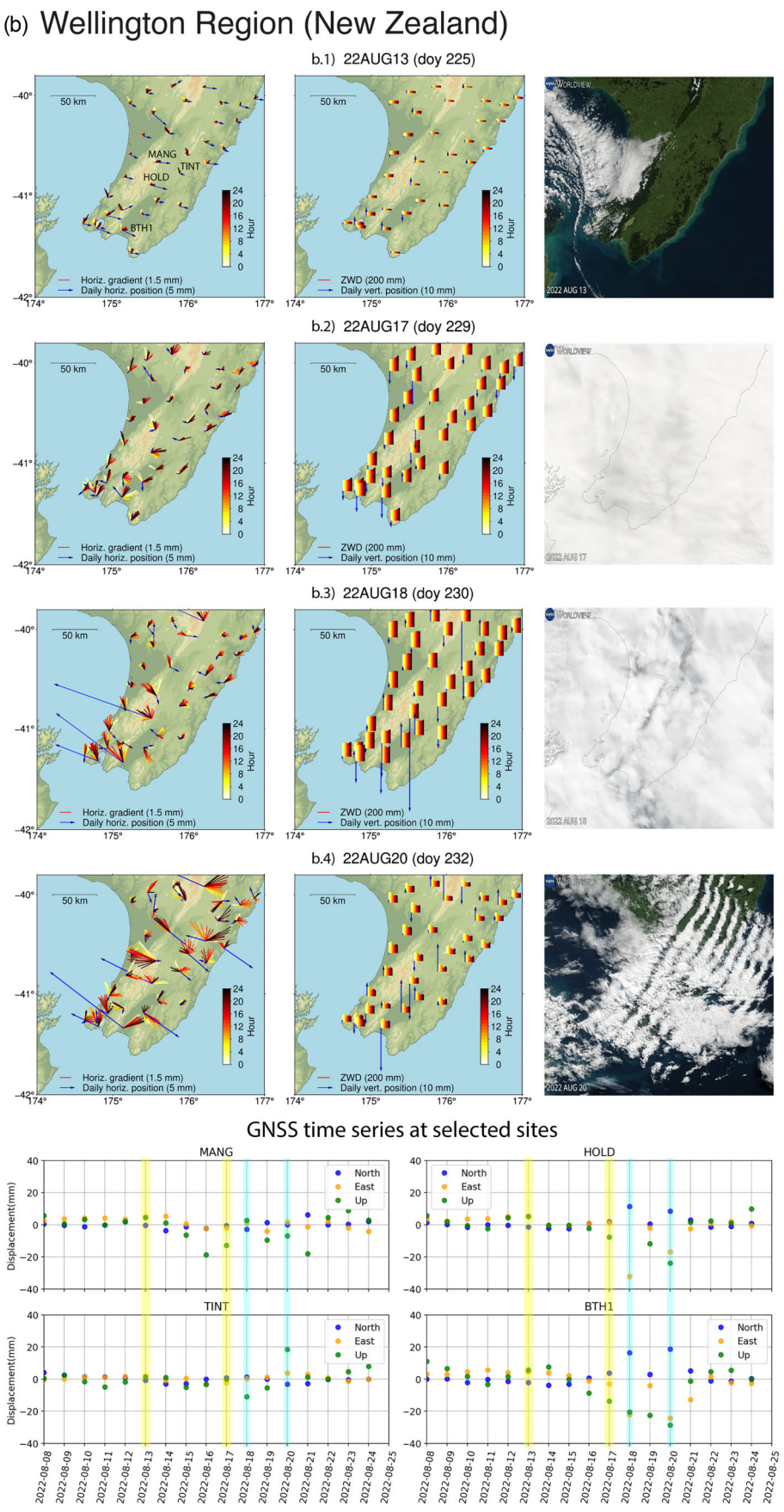

Figure 6. Continued.

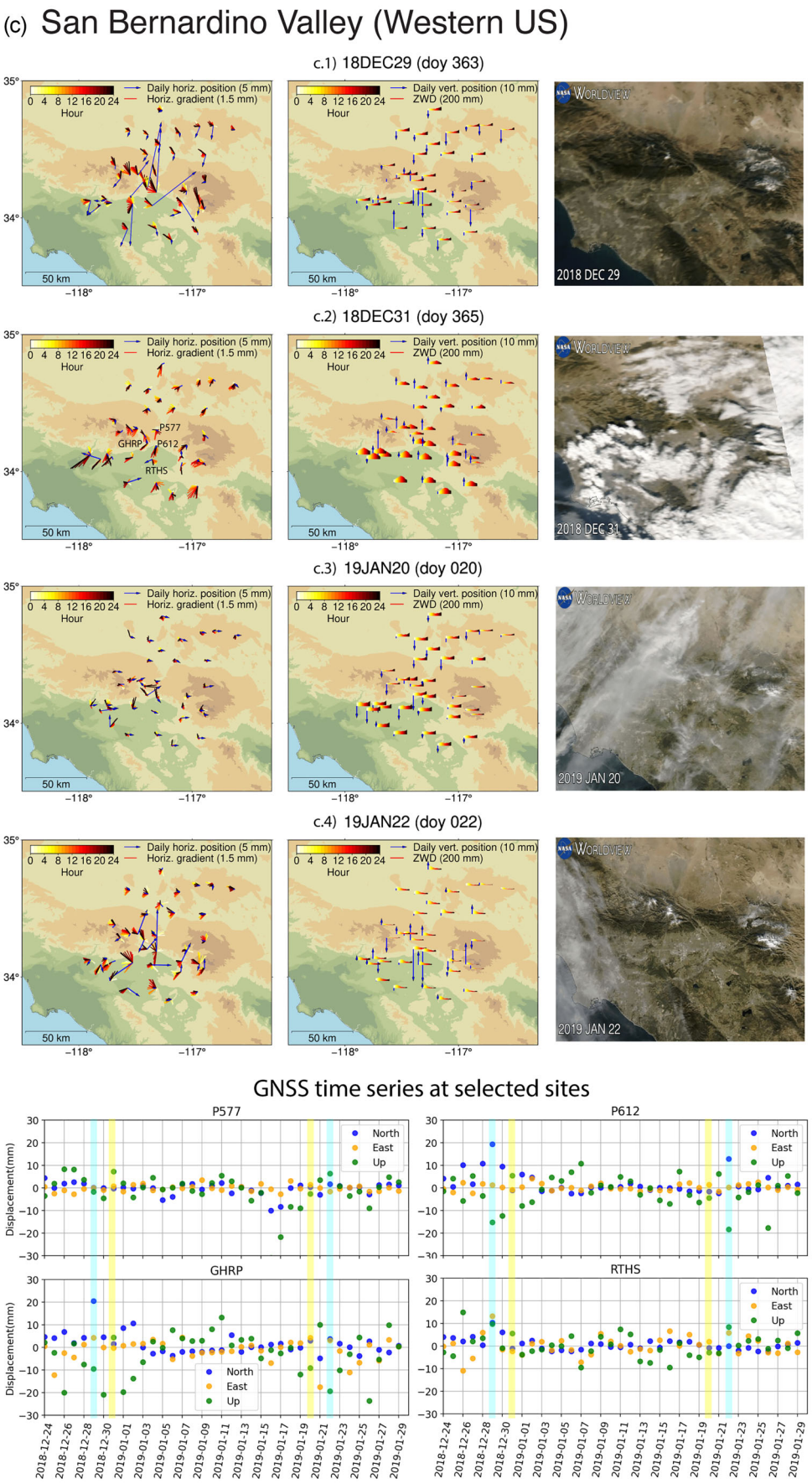

Figure 6. Continued.

Grey 2023, 2026; L. Grey 2024), the Wairarapa and Hawkes Bay regions in North Island of New Zealand (G. Hookings 1968) (geographic locations indicated in Figs 2, 3 and 4). Southern Island in New Zealand, is also known for the formation of lee waves due to strong winds flowing across the Southern Alps (T.P. Lane *et al.* 2000; J.J. Metz *et al.* 2020). Our results show some high-skewness GNSS sites in this area (Fig. 3), however, the low density and scattered location of these sites make it challenging to determine reliable patterns of position errors.

The main features of skewed outliers identified in our analysis at both large and local scales are consistent with the findings of the aforementioned studies. In particular, the local-scale features we highlight in Section 4.2—such as the changes in the direction of horizontal and vertical outliers in the Northern Calabria and Wellington regions—match with the findings of S. Shimada *et al.* (2002), R. Ichikawa *et al.* (2004) and H. Seko *et al.* (2004).

S. Shimada *et al.* (2002), R. Ichikawa *et al.* (2004) and H. Seko *et al.* (2004) also pointed out that, on the lee wave day, the horizontal gradient vectors estimated with the linear gradient model (the method typically employed in routine GNSS processing), are characterized by higher values and opposite direction with respect to the horizontal displacement, pointing to a volume with larger values of water vapour and air density. The tropospheric parameters and MODIS images we collected (Section 4.2 and Fig. 6) show higher values of horizontal gradients at days characterized by position errors, even not always directed opposite to the horizontal displacement, and the occurrence of lee-wave formations.

In summary, the key characteristics of skewed outliers identified in our analysis align with those reported in previous studies about the effects of trapped lee waves on GNSS positioning, supporting this phenomenon as a plausible explanation for several of the observed skewed time-series.

5.1.3 Other possible causes

Other factors exist which could affect GNSS positioning causing high systematic errors and resulting in high skewness time-series. Snow and ice accumulating on GNSS antenna are known to cause significant positioning biases in wintertime at high-mountain sites (R.T.K. Jaldehag *et al.* 1996; K.M. Larson 2013). Their presence indeed affects the carrier phase data through attenuation and scattering of the received signal. Our analysis highlights some groups of sites with high-skewness values in high-mountain areas, which could be associated with this kind of problem. This might be the case of some of the high peaks of the Cascade Volcanic Arc in Western U.S, like Mount St. Helens (Figs 4 and S8–S10 of the Supplementary Material), where the sites at highest elevation are known to be covered in snow and ice in winter (e.g. https://spotlight.unavco.org/station-pages/p698/p698.html).

Multipath is one of the main sources of GNSS positioning errors (e.g. Q. Zhang *et al.* 2024). It is caused by the superposition of direct and reflected signals and it is mainly related to the environment surrounding the station. Multipath is particularly problematic at sites located in complex environments, like vegetated areas, deep canyons, regions in the vicinity of slopes, lakes and buildings, where the presence of unavoidable reflectors leads to the generation of numerous reflected signals. Multipath could be the cause of high skewness at some sites, but, being strongly related to the environment surrounding the station, it seems unlikely to explain the presence of clusters of sites with consistent patterns of highly skewed time-series over distances of several kilometres.

Additionally, in some cases the presence of mountains in the very proximity to a GNSS station may produce less accurate positioning estimates by masking part of the satellites sky view (e.g. S. Gandolfi & L. La Via 2011; J. Han *et al.* 2018). Further analyses are needed for a comprehensive evaluation of the impact of this environmental factor on the formation of asymmetric positioning errors.

5.2 Possible mitigation strategies

Mitigating the occurrence of skewed outliers is not straightforward and largely depends on their underlying causes. Proper installation and ongoing maintenance of GNSS sites are essential to minimize local effects such as multipath or antenna instability (e.g. UNAVCO_Guidelines 2024). In the case of tropospheric-delay related cause, mitigation would primarily involve action at the signal processing stage, as discussed in the following paragraph (Section 5.2.1).

At the post-processing stage, various techniques have been developed to detect and correct position errors in GNSS time-series (e.g. A. Klos *et al.* 2016; X. He *et al.* 2017, and references therein). We investigate a method in the framework of data-driven decomposition (Section 5.2.2).

5.2.1 Processing in the tropospheric-delay context

Although the exact mechanism for lee waves causing systematic positioning errors is not yet fully understood, the studies based on detailed weather models and ray-tracing method (e.g. H. Seko *et al.* 2004; R. Ichikawa *et al.* 2004; L. Grey 2024) showed that lee waves are associated with nonlinear ('wavy') spatial anomalies of dry-air/water-vapour pressure or temperature with relatively small wavelength (few kilometres to few tens of kilometres). These variations cause alternating variations in total air refractivity, affecting the microwave signal path length, potentially leading to positioning errors. Unlike the horizontally stratified or tilted troposphere assumed in standard GNSS models (see Supplementary Table S1 of the Supplementary Material), the tropospheric structure during lee waves cannot be represented by large-scale gradients alone. Consequently, discrepancies between actual and modelled delays result in longer or shorter slant paths and systematic position errors. The non-random character of the large positioning error (i.e. systematically happening on the same side of the time-series) would derive from the spatial regularity of lee waves (W.M. Szeliga & L. Grey 2026), whose location and wavelength are mainly controlled by the topography's height and width (R.S. Scorer 1949).

The mitigation of the effects of the relatively small-scale tropospheric perturbation associated with lee waves is not straightforward and still object of study. H. Seko *et al.* (2004) showed a reduction of horizontal and vertical position errors assuming a 'second-order model', which adds second-order terms to the horizontal gradient parameters, therefore allowing to account for the further curvature of the tropospheric delay. S. Masoumi *et al.* (2017) developed enhanced estimates of tropospheric refractivity gradients (directional model of gradients) in GNSS data processing and applied it to the skewed GNSS time-series

Table 2. Skewness values and number of outliers of the time-series generated by *GispyX* under different scaling factors for the tropospheric random walk constraint.

		Fact 1	Fact 2	Fact 4	Fact 8
REND (Central-Southern Italy)					
Skewness	north : -0.837 ± 0.196	-0.831 ± 0.155	-0.842 ± 0.159	-0.867 ± 0.157
	east: -2.839 ± 0.203	-2.904 ± 0.175	-2.940 ± 0.183	-2.991 ± 0.179
	up: -1.614 ± 0.240	-1.706 ± 0.244	-1.570 ± 0.246	-1.573 ± 0.292
#outliers	north: 136	129	123	117
	east: 348	363	356	353
	up: 196	197	185	169
CAR1 (Central-Southern Italy)					
Skewness	north: -0.454 ± 0.132	-0.410 ± 0.130	-0.438 ± 0.128	-0.454 ± 0.132
	east: -2.587 ± 0.142	-2.601 ± 0.152	-2.566 ± 0.152	-2.527 ± 0.151
	up: -1.044 ± 0.211	-1.085 ± 0.219	-1.060 ± 0.204	-1.045 ± 0.191
#outliers	north: 215	204	196	211
	east: 558	549	561	550
	up: 242	246	240	228

highlighted by K. Materna (2014) in central Sierra Nevada. This resulted in a reduction in position outliers, but mainly on the vertical component, with minimal impact on the horizontal ones, which are the most severely affected.

Recently, Z.M. Young *et al.* (2024) showed that the root mean square and the repeatability of the residual vertical time-series can be improved by loosening the random walk constraint of the tropospheric parameters within a linear gradient model. We test this approach to verify whether it could turn out effective for asymmetric outliers mitigation. We consider two sites characterized by high-skewness (in the East component) in the Northern Calabria Region (CAR1 and REND, location in Fig. 2c) and we reprocess the time-series with the *GipsyX* software (W. Bertiger *et al.* 2020) using looser values for the random walk constraint of tropospheric parameters. Analogously to Z.M. Young *et al.* (2024), we modify the value of the random walk constraint for ZWD and horizontal gradients by multiplying the default value ($3\text{mm}/\sqrt{\text{hr}}$ for ZWD and $0.3\text{mm}/\sqrt{\text{hr}}$ for gradients) by scaling factors of 2, 4 and 8. We then repeat the computation of skewness value and outliers number on the residual time-series, without discarding the data exceeding eight times IQR (Section 3). For both sites, increasing the scaling factor results in minor changes of skewness values, within the associated uncertainty (Table 2 and Supplementary Fig. S18 of the Supplementary Material). In particular, the skewness and outliers number in the East component do not change notably with increasing scaling factor, while there is about 14 per cent decrease in outliers numbers of North and Up components for REND. Even if based on only two test-cases, our results indicate that this strategy is not effective for mitigating the occurrence of asymmetric outliers (Section 4.2).

Lee waves create alternating changes in total air refractivity that affect the effective signal path length. This makes the cutoff angle a potentially important processing parameter, as it determines how much of the signal travels through the atmosphere. Following K. Materna (2014), we attempt a rough estimation of the number of visible lee waves wavelengths from a GNSS station located at a few hundred metres above sea level, as in Northern Calabria (Fig. 2c). Assuming the altitude of the trapping layer, which stops the vertical propagation of trapped lee waves, at about 5–8 km altitude (K. Materna 2014), and a typical cut-off angle of 10°, the edge of visibility of the trapping layer surface from a GNSS site is about 30–45 km away in either direction. Therefore, for typical lee waves with 10–15 km wavelengths, 4–9 wavelengths would be visible to a GNSS station across the entire sky. Increasing/decreasing the cut-off angle would decrease/increase the number of visible wavelengths. We examine the impact of varying the cut-off angle (from 0° to 25°) focusing on a week surrounding a known position error day (2010 March 31, Fig. 6a.2) in Northern Calabria region. The analysis is conducted in the *INGV_BERNESE* framework at the sites CAR1, TVRN and LUZZ, respectively located on the west, middle and east side of the valley (Figs 2c and S19 of the Supplementary Material). The observed results are potentially interesting, but not straightforward and conclusive. Increasing the cut-off angle progressively decreases (up to 50 per cent) the westward position error amplitude at CAR1. The east component of LUZZ is not significantly affected, showing minor changes, whereas the vertical position increases first and then decreases (up to about 80 per cent). The north and vertical components of TVRN experience a direction inversion for cutoff-angle values $\geq 15°$ (southward to northward and upward to downward). Assuming lee waves as responsible of the position error, these changes would depend on the fact that increasing the cut-off angle progressively removes a part of the troposphere anomalies seen by the GNSS site, with the effect depending on the site location with respect to the wavy troposphere. Expectedly, the cut-off angle variation also affects the results at non-outliers days, mostly in the vertical component (up to 20 mm in TRVN). A deeper understanding of the outcome of this test would require further detailed analysis, e.g. involving the computation of perturbed refractivity patterns related to the lee wave formation (L. Grey 2024).

5.2.2 Post-processing

Some studies using GNSS time-series for seismic, volcanic, and hydrologic deformation analysis in different locations of Western U.S. and New Zealand (A. Gualandi *et al.* 2020; F. Silverii *et al.* 2021; S. Michel *et al.* 2022; A. Gualandi 2025; S. Michel *et al.* 2025) have shown that multivariate data-driven decomposition techniques, such as the variational Bayesian independent component analysis (vbICA) (A. Gualandi *et al.* 2016), can effectively identify and isolate asymmetric outliers across multiple time-series. Notably, these previous studies showed that vbICA could extract independent components able to capture these asymmetric

outliers by using as input not the residual time-series, but GNSS position time-series only corrected for a linear trend and offsets.

We test the vbICA algorithm on our data set implementing the decomposition on the residual time-series obtained as described in Section 3, for consistency with the skewness analysis. Since preliminary tests with 3-dimensional data did not show clear results for the vertical component, we focus solely on the horizontal components. For simplicity's sake—and given that earlier analyses showed similar results across different data sets—we consider one data set for each region in our decomposition (*INGV_GIPSY* for Central-Southern Italy, *ENS* for New Zealand, and *JPL* for Western U.S.). The vbICA analysis results in four components for Central-Southern Italy and Western U.S., and five components for New Zealand (Fig. 7 and Supplementary Fig. S20 of the Supplementary Material). In all three regions there are two components (Fig. 7) whose temporal evolution clearly highlights asymmetric positioning errors, and whose spatial distribution shows similar features to those highlighted by the skewness analysis (Section 4.1), that is, higher amplitude at sites located close to/in mountainous areas with mostly perpendicular orientation respect to the main topographic trend. It is worth noting that the splitting of the asymmetric signal into multiple vbICA components was also observed in previous studies (A. Gualandi *et al.* 2020; S. Michel *et al.* 2022, 2025; A. Gualandi 2025), meaning that multiple components are likely needed to fully capture the features of the sources causing the asymmetric outliers in GNSS time-series, particularly when dealing with large regions. This is likely due to the fact that the factors causing asymmetric outliers can affect different areas at different times and that the algorithm is not designed to deal with moving sources. We discuss this further and provide additional details about the vbICA approach in the Supplementary Material (Text S1).

While the skewness analysis considers each component of each time-series separately, data-driven decompositions as vbICA take into account all data at the same time and aim to extract the main, underlying signal sources that are common to multiple time-series across the studied area. We show that the application of vbICA successfully isolated the asymmetric outliers in the residual time-series and confirmed the main features previously highlighted by the skewness analysis (Section 4.1). Based on our results and on the ones of the aforementioned studies (A. Gualandi *et al.* 2020; F. Silverii *et al.* 2021; S. Michel *et al.* 2022; A. Gualandi 2025; S. Michel *et al.* 2025), we suggest that this approach could represent an efficient method to isolate the signals of interest (e.g. earthquake- or volcano-related transient deformation) from skewed outliers in multiple GNSS time-series, without the necessity of the prior filter-removal step applied here. It should be noted, however, that, since vbICA is a data-driven approach, its capacity to effectively isolate the signal of interest from skewed outliers strongly depends on the input data quality. Dense GNSS networks and long, complete time-series are required to maximize its effectiveness.

6 CONCLUSIONS

We conduct a large-scale (hundreds–thousands of km) analysis of asymmetric positioning errors in GNSS time-series, using data from thousands of sites processed by multiple centres. We identify robust, recurring patterns across three major world regions. We confirm known spatiotemporal features of skewed outliers in the Western U.S. (K. Materna 2014) and reveal similar behaviour in Central-Southern Italy and New Zealand. In all regions, skewed outliers occur mainly in mountainous areas and predominantly affect horizontal components, with a consistent directional bias related to the local topography geometry. In some cases, vertical components show alternating skewness patterns at local scales. These effects appear across data sets, independently of processing strategy or instrumental setup. The key characteristics of asymmetric outliers identified in our analysis align with those of previous studies that link the occurrence of skewed position errors to uncorrected delays from nonlinear tropospheric phenomena, particularly trapped lee waves, suggesting the anisotropic tropospheric processes as the primary source of the persistently skewed time-series observed in some areas.

Standard GNSS processing typically estimates tropospheric zenith path delays by projecting slant delays from each satellite to the zenith direction using an elevation-dependent mapping function. Previous attempts involving more complex models for tropospheric delay estimation in GNSS processing have not yet yielded conclusive results (e.g. H. Seko *et al.* 2004; S. Masoumi *et al.* 2017). We test the approach of loosening the random walk constraint within a linear gradient model (Z.M. Young *et al.* 2024), but this does not appear effective in mitigating the occurrence of asymmetric outliers. Further investigation is required, and high-resolution tropospheric modelling—both in time and space—may be necessary to achieve meaningful improvements.

Several questions about the observed phenomenon and its effects on GNSS time-series still remain unanswered, such as why outliers appear on some days with lee waves but not on others, or why nearby sites do not always exhibit outliers on the same day (K. Materna 2014; L. Grey 2024). Future research on this topic should focus both into a deeper understanding of the phenomenon and into investigations of effective methods to mitigate its impact. Additional research should also involve other mountainous regions equipped with dense GNSS networks to determine if asymmetric outliers occur, and assess whether their presence is linked to specific topographic characteristics (e.g. shape, orientation and slope) or meteorological conditions that influence the formation of lee waves. Further understanding could also benefit other techniques of displacement measurement which are strongly affected by tropospheric delay, such as Interferometric Synthetic Aperture Radar (InSAR) (Y. Kinoshita *et al.* 2017).

The main results of our skewness analysis were also confirmed by a multivariate data-driven decomposition (vbICA), which considers all time-series at the same time and extracts the main features common to multiple time-series. When trying to understand the cause of the observed phenomenon, our study—like the previous ones on this topic—faces however an inevitable limitation related to the complexity of the process at hand, and with the high number of GNSS sites and of observation epochs: at some point the analysis must necessarily focus on a limited number of specific cases (i.e. selected sites and dates). It is therefore expected that other phenomena, such as multipath, snow accumulation on GNSS antennas or masked sky visibility, may significantly contribute in causing large asymmetric outliers, and specific investigations are required to quantify their impact.

Our findings indicate that centimetric errors (up to few cm) are often present in daily position time-series close to mountainous regions, independently of the adopted processing

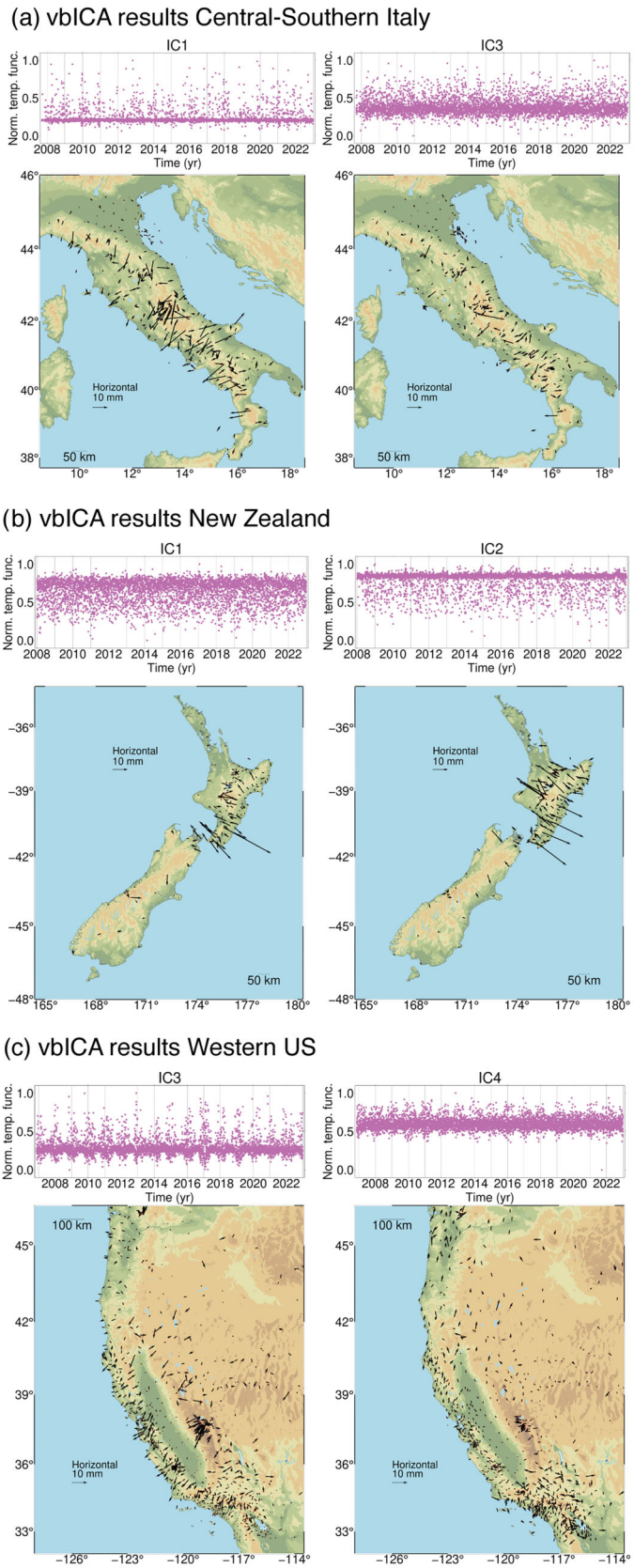

Figure 7. vbICA decomposition results for the three studied areas (selected components highlighting asymmetric outliers; the remaining components are shown in Supplementary Fig. S20 of the Supplementary Material). Each panel represents a vbICA component, showing the temporal functions (top) and spatial distributions (bottom) of each component. The displacement at each GNSS site can be reconstructed by multiplying the spatial value at the site and the corresponding temporal function.

strategy. These regions are typically either volcanic or tectonically active and GNSS data can be fundamental for the estimation of interseismic strain, and earthquake or volcano-related deformation (e.g. D. Hill *et al.* 2020; R. Nucci *et al.* 2025). An important implication is that, before analysing GNSS position time-series for small volcanic or tectonic transients, one should consider the possible presence of these outliers that are likely not related to the physics of the Solid Earth component. This is especially relevant when using short time-series or campaign-based measurements, or when investigating small (millimetric) amplitude and/or short-lived (daily or subdaily) signals. In those cases, it is important to either carefully examine potential error sources and optimize instrumentation placement; or validate, when possible, GNSS data by comparison with ground-based geodetic observations, such as strainmeters and creepmeters; or employ robust post-processing techniques to identify and remove (asymmetric) outliers, such as data-driven decomposition or specific outlier removal techniques.

ACKNOWLEDGMENTS

We thank the Editor Chris Rollins and two anonymous Reviewers for their thorough comments which helped to improve this paper. We are grateful to Nicola D'Agostino (INGV) for providing GNSS time-series for Italy processed with *Gipsy* software, for the help with *GipsyX* tests and for useful discussions. We thank Jade Morton (CU Boulder) for insightful suggestions.

We are grateful to all the personnel involved in the mainteinance of the GNSS networks and in processing the GNSS data.

We used Python and MATLAB for computations and Generic Mapping Tools (P. Wessel *et al.* 2019) for figures.

AUTHOR CONTRIBUTIONS

Francesca Silverii (Conceptualization, Formal analysis, Investigation, Methodology, Software, Supervision, Validation, Visualization, Writing—original draft), Emilie Klein (Data curation, Formal analysis, Validation, Writing—review and editing), Roberto Devoti (Data curation, Formal analysis, Writing—review and editing), Walter Szeliga (Conceptualization, Investigation, Methodology, Writing—review and editing), Sylvain Michel (Methodology, Writing—original draft), Adriano Gualandi (Methodology, Writing—review and editing), and Elisa Trasatti (Methodology, Writing—review and editing)

SUPPORTING INFORMATION

Supplementary data are available at *GJIRAS* online.

Table S1. Information about tropospheric correction strategies applied in the different used data sets.
Table S2. Collected information about GNSS station instrumentation and related data sources.

Table S3. Number of sites associated with different values of horizontal (H) and vertical (V) skewness amplitude. The values in brackets represent the percentage respect to the total number of selected sites for each data set (see Table 1 in the main text).
Table S4. Values of vbICA hyperparameters (Text S1). Their nomenclature and description are taken from Gualandi & Liu (2021).

Table S5. Skewness values of the temporal trends associated with the independent components extracted through vbICA analysis.

Table S6. Results of cross-correlation test (and related time lag and *p*-value) between the derivative of an asymmetry-related vbICA components (dICx) and the remaining components. Bold fonts indicate the components combinations with best combinations, for each region, of high correlation and low *p*-value.

Figure S1. Comparison of skewness results obtained using different values (6, 8 and 20) of the multiplicative factor used for the removal of large isolated outliers in the raw time-series. Associated skewness uncertainty values are also represented (as 60 per cent CI ellipse). Compared to the selected one (8), using a more conservative value of the multiplicative factor (6—panels a to d) leads to consistent results (with lower skewness values). On the contrary, using a less conservative value (20—panels e to h) leads to mostly consistent results (with higher skewness values) at sites already characterized by high skewness, but causes several large skewness values at randomly distributed sites, likely related to the presence of isolated singletons in the time-series. Darker and lighter vector colours in left panels (a, c, e, g) highlight sites with respectively skewness higher/lower than 1. Right panels (b, d, f, h) represent the difference between the skewness obtained through modified factors (respectively 6 and 20) and the reference one (8). Region: Central-Southern Italy, data set: *INGV_GIPSY*.
Figure S2. Large-scale skewness analysis results. Darker and lighter vector colours (panels a, c) highlight sites with respectively skewness higher/lower than 1. Vectors are plotted with associated 60 per cent CI ellipse. Region: Central-Southern Italy, data set: INGV_GIPSY.
Figure S3. Same as Fig. S2. Region: Central-Southern Italy, data set: *INGV_BERENSE*.
Figure S4. Same as Fig. S2. Region: Central-Southern Italy, data set: *NGL*.
Figure S5. Same as Fig. S2. Region: New Zealand, data set: *ENS*.
Figure S6. Same as Fig. S2. Region: New Zealand, data set: *GNS*.
Figure S7. Same as Fig. S2. Region: New Zealand, data set: *NGL*.
Figure S8. Same as Fig. S2. Region: Western US, data set: *JPL*.
Figure S9. Same as Fig. S2. Region: Western US, data set: *SOPAC*.
Figure S10. Same as Fig. S2. Region: Western US, data set: *NGL*.
Figure S11. Examples of (residual) time-series and related features. Each sub-figure (A, B, C) is related to each of the three selected local-scale areas (see Section 4.2 of the main text), showing the comparison between the time-series of two different sites (panels 1), or of the same site obtained through different processing techniques (panels 2). Sub-panels d) shows the outliers (data over 1.5∗IQR) distribution during the year considering all components (north, east and vertical). See Figs S15–S17 or Figs 2–4 of the main text for sites location.
Figure S12. Maps showing the spatial distribution of several GNSS station features for Central–Southern Italy (see Table S2). Only the sites marked as selected are shown (i.e. associated with time–series with duration $\geq$3 yr and completeness $\geq$60 per cent, see Table 1 in the main text). The features in panels a–c refer to the most recent site configuration. For the quantitative features, we also plot the feature value against the associated skewness values (panels g, h).
Figure S13. Maps showing the spatial distribution of several GNSS station features for New Zealand (see Table S2). Only the

sites marked as selected are shown (i.e. associated with time-series with duration ≥ 3 yr and completeness ≥ 60 per cent, see Table 1 in the main text). The features in panels a–c refer to the most recent site configuration. For the quantitative features, we also plot the feature value against the associated skewness values (panels g, h).

Figure S14. Maps showing the spatial distribution of several GNSS station features for Western U.S. (see Table S2). Only the sites marked as selected are shown (i.e. associated with time-series with duration ≥ 3 yr and completeness ≥ 60 per cent, see Table 1 in the main text). The features in panels a–c refer to the most recent site configuration. For the quantitative features, we also plot the feature value against the associated skewness values (panels g, h).

Figure S15. Same as Fig. S12, local-scale focus.

Figure S16. Same as Fig. S13, local-scale focus.

Figure S17. Same as Fig. S14, local-scale focus.

Figure S18. Residual time-series of CAR1 (A) and REND (B) sites (Central-Southern Italy) obtained using *GispyX* software with different scaling factors for the random walk constraint of tropospheric parameters. The different panels show the same features as Fig. S11.

Figure S19. Test of cutoff angle variation (0○ to 25○) at three sites in Calabria Region (CAR1, TRVN and LUZZ) on 7 d including the high position error day (2010 March 31, as in Fig. 6a.2 of the main text). The numeric values in the legend represent the root mean square values of each time-series.

Figure S20. vbICA decomposition results for the three studied areas (components not related to asymmetric outliers). Each panel represents a vbICA component, with the top and bottom plots respectively showing the temporal functions and spatial distributions of each component. To reconstruct the displacement at a GNSS site, multiply the spatial value at the site and the corresponding temporal function.

Figure S21. Lomb–Scargle periodograms associated with the temporal functions of the vbICA components shown in Fig. 7 of the main text and in Fig. S20.

Please note: Oxford University Press is not responsible for the content or functionality of any supporting materials supplied by the authors. Any queries (other than missing material) should be directed to the corresponding author for the paper.

DATA AVAILABILITY

We used publicly available GNSS time-series from: Nevada Geodetic Laboratory, University of Nevada (http://geodesy.unr.edu/index.php – last accessed April 2024) G. Blewitt *et al.* (2018); GeoNet (https://www.geonet.org.nz/data/types/geodetic—last accessed December 2022) GNS Science (2000); Scripps Institution of Oceanography's Orbit and Permanent Array Center (http://garner.ucsd.edu/pub/measuresESESES_products/Timeseries/WesternNorthAmerica/ – last accessed June 2023); NASA Jet Propulsion Laboratory (http://garner.ucsd.edu/pub/measuresESESES_products/Timeseries/WesternNorthAmerica/ – last accessed November 2023) (ESESES MEaSUREs 2023).

The GNSS time-series processed at Istituto Nazionale di Geofisica e Vulcanologia (INGV) through the *Bernese* software are available at https://webring.gm.ingv.it/index.php/data-analysis-and-product/ (Devoti R., Pietrantonio G. 2025). The GNSS time-series processed at Istituto Nazionale di Geofisica e Vulcanologia (INGV) through the *Gipsy-Oasis II* and the *GipsyX* software are available at https://webring.gm.ingv.it/index.php/data-analysis-and-product/. The GNSS time-series processed at Ecole normale supérieure, Paris (ENS) using GAMIT/GLOBK/PYACS are available through the Geodesy Plotter (2025). More information about the processing developed at ENS can be found in S. Michel *et al.* (2025).

Information about the GNSS station instrumentation was collected from NGL (http://geodesy.unr.edu/monuments/MonumentTable.txt), GeoNet - GNS Science (https://data.geonet.org.nz/gnss/sitelogs/), SOPAC (http://sopac-csrc.ucsd.edu/index.php/gambit-globk/), and INGV metadata database (file INGV_station_metadata_sel.csv in the Supplementary Material), see also Supplementary Table S2 of the Supplementary Material.

The tropospheric products files from Nevada Geodetic Laboratory, University of Nevada, are available at http://geodesy.unr.edu/gps_timeseries/trop/.

We acknowledge the use of imagery from the NASA Worldview application (https://worldview.earthdata.nasa.gov), part of the NASA Earth Science Data and Information System (ESDIS).

The results of the skewness analysis and a Python Jupyter Notebook to perform the skewness analysis are provided in the supplementary directory *Silverii_et_al_results.zip*

REFERENCES

Beavan, J., 2005. Noise properties of continuous GPS data from concrete pillar geodetic monuments in New Zealand and comparison with data from U.S. deep drilled braced monuments, *J. geophys. Res.: Solid Earth,* **110**(B8), e2005JB003642. doi:10.1029/2005JB003642.

Bertiger, W. *et al.*, 2020. GipsyX/RTGx, a new tool set for space geodetic operations and research, *Adv. Space Res.,* **66**(3), 469–489.

Blewitt, G. *et al.*, 2013. Terrestrial reference frame NA12 for crustal deformation studies in North America, *J. Geodyn.,* **72,** 11–24.

Blewitt, G., Hammond, W.C. & Kreemer, C., 2018. Harnessing the GPS data explosion for interdisciplinary science. [Dataset], *Eos*. Available at: https://eos.org/science-updates/harnessing-the-gps-data-explosion-for-interdisciplinary-science.

Bock, Y. & Melgar, D., 2016. Physical applications of GPS geodesy: a review, *Rep. Prog. Phys.,* **79**(10), 106801. doi:10.1088/0034-4885/79/10/106801.

Devoti R.,, Pietrantonio G. 2025. Time Series of GNSS positions, INGV Bernese Data Processing (BEPOS) [Data set]. Istituto Nazionale di Geofisica e Vulcanologia (INGV)

Durran, D., 2003. Lee waves and mountain waves, in *Encyclopedia of Atmospheric Sciences,* pp. 1161–1169, ed. Holton, J.R., Academic Press.

Durran, D.R., 1986. Mountain Waves, in *Mesoscale Meteorology and Forecasting,* pp. 472–492, ed. Ray, P.S., American Meteorological Society.

Efron, B. & Tibshirani, R., 1986. Bootstrap methods for standard errors, confidence intervals, and other measures of statistical accuracy, *Stat. Sci.,* **1**(1), 54–75.

ESESES MEaSUREs Daily GNSS Geodetic Displacement Time Series [online]. *Available from the NASA Crustal Dynamics Data Information System DAAC, Greenbelt, MD,* USA.doi:10.5067/GNSS/gnss_daily_displacement_timeseries_001.

Gandolfi, S. & La Via, L., 2011. SKYPLOT_DEM: a tool for GNSS planning and simulations, *Appl. Geomat.,* **3,** 35–48.

Gegout, P., Biancale, R. & Soudarin, L., 2011. Adaptive mapping functions to the azimuthal anisotropy of the neutral atmosphere, *J. Geodesy,* **85**(10), 661–677.

Geodesy Plotter, 2025. Solution nz_gnss_solens. Available at: https://www.poleterresolide.fr/geodesy-plotter/#/?bounds=164.78393554687503,-45.83645405018772,185.24047851562503,-35.362176059146805&expand=1&solution=NZ_GNSS_solENS, [data set].

GNS Science, 2000. GeoNet Aotearoa New Zealand Continuous GNSS Network Time Series Dataset, [Dataset], GNS Science, GeoNet.

Gobron, K. *et al.*, 2024. Anatomy of the spatiotemporally correlated noise in GNSS station position time series, *J. Geodesy,* **98**(5), 34. doi:10.1007/s00190-024-01848-z.

Grey, L., 2024. GNSS Radio Propagation Through Trapped Atmospheric Lee Waves in the San Bernardino Valley, CA. All Master's Theses. 1940.

Gualandi, A. & Liu, Z., 2021. Variational Bayesian independent component analysis for InSAR displacement time-series with application to Central California, USA, *J. geophys. Res.: Solid Earth,* **126**(4), e2020JB020845. doi:10.1029/2020JB020845.

Gualandi, A., 2025. Near real-time Cascadia slow slip events, *Geophys. J. Int.,* **242**(2), ggaf198. doi:10.1093/gji/ggaf198.

Gualandi, A., Liu, Z. & Rollins, C., 2020. Post-large earthquake seismic activities mediated by aseismic deformation processes, *Earth planet. Sci. Lett.,* **530,** 115870. doi:10.1016/j.epsl.2019.115870.

Gualandi, A., Serpelloni, E. & Belardinelli, M., 2016. Blind source separation problem in gps time series, *J. Geodesy,* **90**(4), 323–341.

Han, J., Huang, G., Zhang, Q., Tu, R., Du, Y. & Wang, X., 2018. A new Azimuth-Dependent Elevation Weight (ADEW) model for real-time deformation monitoring in complex environment by Multi-GNSS, *Sensors,* **18**(8), 2473. doi:10.3390/s18082473.

He, X. *et al.*, 2017. Review of current GPS methodologies for producing accurate time series and their error sources, *J. Geodyn.,* **106,** 12–29.

Hill, D. *et al.*, 2020. Post-1978 tumescence at Long Valley Caldera, California: a geophysical perspective, *J. Volc. Geotherm. Res.,* **400,** 106900. doi:10.1016/j.jvolgeores.2020.106900.

Hookings, G., 1968. The lee wave systems of New Zealand, p. 9, OSTIV Publications.

Ichikawa, R., Seko, H. & Bevis, M.G., 2004. An evaluation of geodetic positioning error simulated using a mesocale nonhydrostatic model, in *Remote Sensing Applications of the Global Positioning System*. Vol. **5661,** SPIE.

Jaldehag, R.T.K. *et al.*, 1996. Geodesy using the Swedish Permanent GPS Network: Effects of snow accumulation on estimates of site positions, *Geophys. Res. Lett.,* **23**(13), 1601–-1604.

Kinoshita, Y., Morishita, Y. & Hirabayashi, Y., 2017. Detections and simulations of tropospheric water vapor fluctuations due to trapped lee waves by ALOS-2/PALSAR-2 ScanSAR interferometry, *Earth Planets Space,* **69**(1), 104. doi:10.1186/s40623-017-0690-7.

Klos, A. *et al.*, 2016. On the handling of outliers in the GNSS time series by means of the noise and probability analysis, in Rizos, C. & Willis, P., eds, *IAG 150 Years,* pp. 657–664, Springer International Publishing.

Landskron, D., Hofmeister, A. & Böhm, J., 2017. Refined tropospheric delay models for CONT11, in van Dam, T., ed., *REFAG 2014,* pp. 65–69, Springer International Publishing.

Lane, T.P. *et al.*, 2000. Observations and numerical modelling of mountain waves over the Southern Alps of New Zealand, *Q. J. R. Meteor. Soc.,* **126**(569), 2765–2788.

Langbein, J. & Svarc, J.L., 2019. Evaluation of temporally correlated noise in global navigation satellite system time series: Geodetic monument performance, *J. geophys. Res.: Solid Earth,* **124**(1), 925–942.

Larson, K.M., 2013. A methodology to eliminate snow- and ice-contaminated solutions from GPS coordinate time series, *J. geophys. Res.: Solid Earth,* **118**(8), doi:10.1002/jgrb.50307.

Li, X. *et al.*, 2023. Towards millimeter-level accuracy in GNSS-based space geodesy: a review of error budget for GNSS precise point positioning, *Surv. Geophys.,* **44**(6), 1691–1780.

Maronna, R.A., Martin, R.D. & Yohai, V.J., 2006. *Robust Statistics: Theory and Methods,* Wiley Series in Probability and Statistics, John Wiley & Sons Ltd.

Masoumi, S. *et al.*, 2017. A directional model of tropospheric horizontal gradients in Global Positioning System and its application for particular weather scenarios, *J. geophys. Res.: Atmospheres,* **122**(8), 4401–4425.

Materna, K., 2014. *Analysis of atmospheric delays and asymmetric positioning errors in the global positioning system,* thesis, MIT

Meindl, M. *et al.*, 2004. Tropospheric gradient estimation at CODE: results from global solutions, *J. Meteor. Soc. Jpn Ser II,* **82**(1B), 331–338.

Metz, J.J., Durran, D.R. & Blossey, P.N., 2020. Unusual trapped mountain lee waves with deep vertical penetration and significant stratospheric amplitude, *J. Atmos. Sci.,* **77**(2), 633–646.

Michel, S. *et al.*, 2022. Searching for transient slow slips along the San Andreas fault near Parkfield using independent component analysis, *J. geophys. Res.: Solid Earth,* **127**(6), e2021JB023201. doi:10.1029/2021JB023201.

Michel, S. *et al.*, 2025. 14 Years of slip on the Hikurangi subduction zone, *J. geophys. Res.: Solid Earth,* **130,** e2024JB030865. doi:10.1029/2024JB030865.

Nucci, R. *et al.*, 2025. Geodetic strain rates and seismicity rates along the Apennines (Italy), *J. geophys. Res.: Solid Earth,* **130**(2), e2024JB029848. doi:10.1029/2024JB029848.

Rizos, C., Altamimi, Z. & Johnson, G., 2020. *Global Geodesy and Reference Frames, Chap 27,* pp. 717–739, eds Jade, Y. T. M.et al., John Wiley and Sons, Ltd.

Rousseeuw, P.J. & Leroy, A.M., 1987. *Robust Regression and Outlier Detection,* Wiley Series in Probability and Statistics, John Wiley & Sons, Inc.

Scorer, R.S., 1949. Theory of waves in the lee of mountains, *Q. J. R. Meteor. Soc.,* **75**(323), 41–56.

Seko, H., Nakamura, H. & Shimada, S., 2004. An evaluation of atmospheric models for GPS data retrieval by output from a numerical weather model, *J. Meteor. Soc. Jpn Ser II,* **82**(1B), 339–350.

Shimada, S., Seko, H., Nakamura, H., Aonashi, K. & Herring, T. A., 2002. The impact of atmospheric mountain lee waves on systematic geodetic errors observed using the Global Positioning System, *Earth Planets Space,* **54**(4), 425–430.

Silverii, F., Pulvirenti, F., Montgomery-Brown, E., Borsa, A.A. & Neely, W.R. 2021. The 2011-2019 Long Valley Caldera inflation: New insights from separation of superimposed geodetic signals and 3D modeling, *Earth planet. Sci. Lett.,* **569,** 117055. doi:10.1016/j.epsl.2021.117055.

Stamps, D.S. & Kreemer, C., 2024. Open access GNSS data for studies of the lithosphere, *Geochem. Geophys. Geosyst.,* **25**(7), e2024GC011567. doi:10.1029/2024GC011567.

Szeliga, W.M., Grey, L. & Durran, D.R., 2022. GNSS Radio Propagation through Trapped Atmospheric Lee Waves in the San Bernardino Valley, CA, in *AGU Fall Meeting 2022,* Chicago, IL, USA.

Szeliga, W.M. & Grey, L., 2023. Preliminary results from observation of electromagnetic scintillation due to turbulence created by atmospheric lee waves, in *AGU Fall Meeting 2023,* San Francisco, CA, USA.

Szeliga, W.M. & Grey, L., 2026. Perturbations to horizontal GNSS position time series by atmospheric lee waves in the San Bernardino Valley, California, *J. Geodetic Sci.,* In Press.

UNAVCO_Guidelines, 2024. UNAVCO Resources: Permanent GPS/GNSS Stations. Available at: https://www.google.com/search?q=pbo+guidelines+gnss+installationandoq=pbo+guidelines+gnss+installationandgs_lcrp=EgZjaHJvbWUyBggAEEUYOTIHCAEQIRigATIHCAIQIRigATIHCAMQIRigAdIBCTEyNzEwajBqN6gCALACAAandsourceid=chromeandie=UTF-8(accessed 13 June 2025).

Wessel, P. *et al.*, 2019. The generic mapping tools version 6, *Geochem. Geophys. Geosyst.,* **20**(11), 5556–5564.

Young, Z.M., Blewitt, G. & Kreemer, C., 2024. Improved GPS tropospheric path delay estimation using variable random walk process noise, *J. Geodesy,* **98**(10), 89. doi:10.1007/s00190-024-01898-3.

Zhang, Q., Zhang, L., Sun, A., Meng, X., Zhao, D. & Hancock, C. 2024. GNSS carrier-phase multipath modeling and correction: a review and prospect of data processing methods, *Remote Sens.,* **16**(1), 189. doi:10.3390/rs16010189.